atmosphere

MDPI

Article

Frontal Wind Field Retrieval Based on UHF Wind Profiler Radars and S-Band Radars Network

Min-Seong Kim [1], Bernard Campistron [2] and Byung Hyuk Kwon [3,*]

[1] Geo-Sciences Institute, Pukyong National University, 45, Yongso-Ro, Nam-Gu, Busan 48513, Korea; willms@nate.com
[2] Laboratoire d'Aérologie, Université de Toulouse III, CNRS, UPS, 31400 Toulouse, France; camb@aero.obs-mip.fr
[3] Department of Environmental Atmospheric Sciences, Pukyong National University, 45, Yongso-Ro, Nam-Gu, Busan 48513, Korea
* Correspondence: bhkwon@pknu.ac.kr; Tel.: +82-51-629-6644

Received: 31 July 2019; Accepted: 12 September 2019; Published: 14 September 2019

Abstract: The three-dimensional wind field (WPR3D) and the multiple WPR3D (M-WPR3D) associated with the passage of a stationary front was derived from observations made by a network of eight wind profiler radars (WPR) being operated by the Korea Meteorological Administration during the summer "Jangma" season. The effectiveness of the WPR3D was determined through numerical model analysis and wind profilers at three sites, and the accuracy of the M-WPR3D was validated by comparing the trajectory of the radiosonde. The discontinuity of the wind field near the frontal interface was clearly retrieved and the penetration of the air mass in the southern front was detected. Compared with either the wind vector of three single wind profiler or a local data assimilation and predication system, the WPR3D wind field showed a wind speed accuracy of approximately 70% at an altitude of 1.5 km and underestimated the wind speed by 0.5–1.5 m s^{-1}. The M-WPR3D with three S-band Doppler radars successfully retrieved the backing wind field as well as the pre-Jangma-frontal jet. The results of this study showed that severe weather can be effectively analyzed using a three-dimensional wind field generated on the basis of a remote sensing network.

Keywords: wind profiler network; triangle method; volume velocity processing; Jangma front; air mass trajectory; atmospheric instability

1. Introduction

The monsoon flow that carries moist air from the Indian Ocean and the Pacific Ocean to East Asia influences the climate of the Korean peninsula. The East Asian monsoon is known as "Jangma" in Korea. The Jangma front in the southern part of Korea is characterized by a midlatitude baroclinic surface tilted toward an upper cold core [1,2] and by a semitropical disturbance with an equivalent barotropic warm core structure in central Korea [2,3]. A long lasting heavy frontal precipitation band, elongated from west to east and embedded in strong winds, is associated with severe natural disasters [4]. Mesoscale convective systems (MCSs) along the front cause heavy rainfall to occur for at least 100 km at the meso-β-scale [5]. This MCSs precipitation over the Korean peninsula is related to a northeastward low-level jet (LLJ) transporting warm and moist air from southern China and a southeastward-moving cold-core mid-tropospheric low [2]. Meso-β-scale convective cells are observed ahead of the front within the warm prefrontal sector known as the squall line [6]. These convective cells are developed when a strong northeastward LLJ intensifies and moisture becomes deeply advected into the sloping frontal zone [7]. The squall line can be identified based on the convective available potential energy (CAPE) and the vertically sheared wind [8–10]. CAPE gives information on the intensity of

convective storms, and the wind shear is useful for determining the magnitude and duration of the squall line. Since heavy rain during Jangma passage in Korea is triggered by dynamic instability rather than by thermal instability [11,12], wind profiler radar observations are very relevant to analyze the three-dimensional structure and development of the squall line.

Wind profiler radars are increasingly being deployed worldwide, providing remarkable information on changing wind fields. These instruments continuously monitor wind fields with a high temporal and spatial resolution (e.g., about 5 min and 100 m respectively for the DEGREWIND PCL1300 UHF (Ultra High Frequency) wind profiler that we use herein). These profilers provide wind fields in clear air or precipitating conditions and the quality of available data has been improved significantly over the past few years. The operational network of wind profilers known as the NOAA National Profiler Network, which provided valuable data for a wide variety of applications (such as data for local and synoptic forecasting models, pollution, or airport monitoring), was implemented in May 1992 and was discontinued in August 2014 [13,14]. In Europe, a first demonstration of the wind profiler network was organized during the COST-76 action in early 1997 as part of the COST WIND initiative for a network demonstration in Europe project [15]. In Asia, the Japan Meteorological Agency operates the Wind profiler Network and Data Acquisition System (WINDAS) of UHF wind profilers [16]. The Korea Meteorological Administration (KMA) has installed nine UHF wind profilers since 2002 [17]. A network of nine UHF Doppler wind profilers at 1.29 GHz and eleven Doppler weather radars (eight in the S-band and three in the C-band) have been deployed all over South Korea, with an average spacing better than 150 km between instruments.

The WPR is optimized for monitoring diurnal wind changes which are important for predicting sever weather and pollution transport [18]. Campistron et al. [19] used four UHF wind profilers, in addition to radiosondes and aircraft profiles, not only to retrieve horizontal fields of the boundary layer depth and turbulence properties but to calculate air trajectories which were compared with trajectories obtained from boundary-layer pressurized balloons. During the international Hydrological Cycle in Mediterranean Experiment (HyMeX) field campaign, three Very High Frequency (VHF) profilers and five UHF profilers for the first 0.1–6 km layer with 5 min resolution were deployed along the French Mediterranean coast and Corsica Island. They were used to retrieve the three-dimensional wind field (WPR3D) atmospheric wind fields over the basin, by assuming linearity of the fields inside a limited spatial and temporal domain. The 3D wind fields derived from the coastline profiler network are representative of the offshore kinematics. This assessment was performed by comparing more than one year of continuous profiler observations during different weather conditions with balloon radio-soundings and in situ aircraft or boundary layer Lagrangian measurements [20]. The WPR3D wind fields over the western Mediterranean Sea are very helpful to understand or model the upstream conditions of heavy precipitation events on mountainous coasts or define boundary conditions for oceanic convection. Saïd et al. [20] noted that the quality of WPR3D depends on the number of radars and their spacing relative to the scale of the atmospheric movements.

In this study, we added S-band Doppler radars on the WPR3D in order to use as a substitute for WPR in areas without WPR. The three-dimensional wind fields retrieved from the KMA-operated wind profiler and S-band weather radar network are compared to the wind fields obtained by a numerical forecasting model as well as upper-air sounding data. We show that the wind field structure of the stationary front can be understood using a network of wind profilers. Moreover, dynamic and thermodynamic diagnosis parameters are proposed based on two types of remote sensing sources—wind profiler networks and radiometers.

2. Data and Method

The WPR3D and multiple WPR3D (M-WPR3D) wind field are composed of eight WPRs and three S-band Doppler radars. Figure 1 shows the whole process of this study. The WPR measures the radial velocity using the Doppler beam swinging (DBS) method. The WPR3D was built and tested around a reference site Chupungnyeong. The wind calculated by the triangular method is compared with

the wind of the single WPR at P0 and with the LDAPS results around P0. Because of the lack of WPR in the southwestern part of the Korean peninsula, the wind field calculated by the volume velocity processing (VVP) method based on a S-band radar at W4 is compared with the WPR3D wind fields on the triangle consisted of P1, P2 and P4. The validation of VVP wind field allows a S-band radar to play a role of single wind profiler for building M-WPR3D. These results of M-WPR3D with S-band radars are compared with the LDAPS wind field.

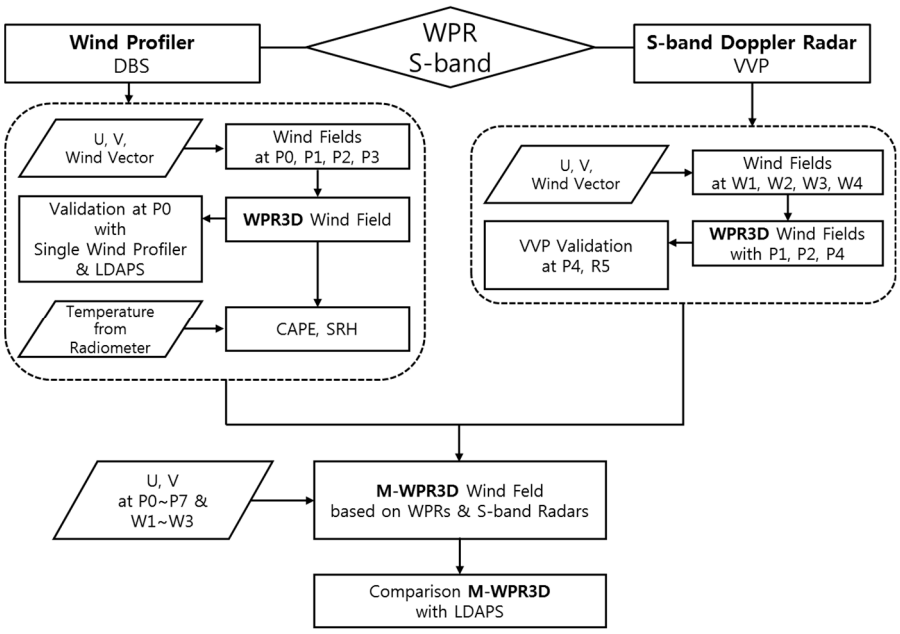

Figure 1. Scheme of the research to construct the three-dimensional wind field (WPR3D) and the multiple WPR3D (M-WPR3D) wind field. Observational sites of 8 wind profilers and 4 S-band radars are indicated by P0–P7 and W1–W4, respectively. R5 is the WPR3D reference point of the triangle P1–P2–P4.

2.1. Data

The DEGREWIND PCL1300 UHF wind profilers of the KMA network, manufactured by the French company Degreane, were being operated continuously during the Jangma episode in 2013. Wind vector data were collected at eight wind profiler sites from 17 June to 22 June 2013. As shown in Figure 2, sites P1 (Gunsan), P2 (Wonju), and P3 (Changwon) are within a 100-km radius circle centered on P0 (Chupungnyeong) the reference site.

The wind profiler radar is configured with operational systems that have five beams with an 8.5° aperture comprising a vertical beam and four oblique ones with 17° zenithal elevations disposed every 90° in the azimuthal direction. During a cycle, these profilers provide about four-min vertical profiles of reflectivity, three components of the wind, the Doppler spectral width, and the spectral skewness. The cycle is composed of low-mode and high-mode data acquisition (Table 1). Data are collected in the vertical, north, east, south, and west directions in low mode for the first two min, followed by the same order in high mode. In this study we used only low-mode data, and the selection of the relevant atmospheric peak in the Doppler spectra was derived with a discrete 128-point Fourier transform window made with a 15-min duration consensus technique based on median filters, thresholds, and vertical and time continuity tests. Particular attention is paid to the detection and decomposition of bimodal peaks resulting from atmospheric and ground clutter echoes.

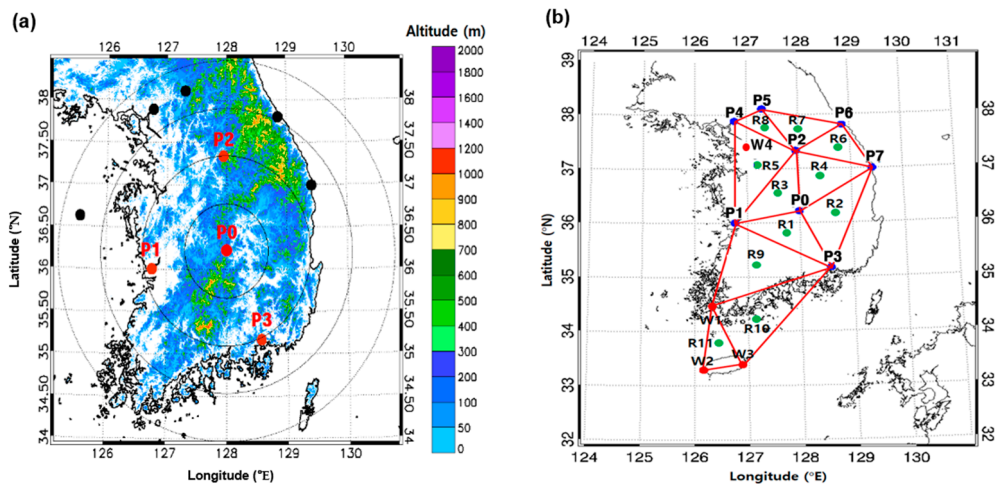

Figure 2. (**a**) positions of wind profilers at the P0, P1, P2, and P3 sites (red points) and the other five wind profilers (black points) superimposed on a topographical map of the South Korea peninsula. Here, 50-km intervals range circles are centered on P0, the profiler reference site. (**b**) a multiple-instrument network constructed by wind profilers (P1–P8) and S-band Doppler weather radars (W1–W4). Green points (R1–R11) indicate the center of the triangle from which the wind fields are derived.

Table 1. Operational configuration of low- and high-mode strategies for the PCL 1300.

Parameter	Low Mode	High Mode	Unit
Frequency	1290	1290	MHz
Peak power	4.5	4.5	kW
Beam number	5	5	
Pulse width	500	1000	ns
Pulse repetition frequency	16	10	kHz
Nyquist velocity	12.84	12.84	m s^{-1}
Number of FFT points	128	128	
Lowest sampled height	72	72	m
Highest sampled height	5100	11700	m
Range resolution	71.68	164.85	m
Number of height gates	71	71	

Doppler weather radar can measure the radial velocity by scattering based on the same principle as the wind profiler, and it can calculate the wind vector through the radial velocity at the three-dimensional coordinates with the altitude, azimuth, and radius. In Figure 1, southwest of the wind profiler observation network on the Korean peninsula is the no-observations area in which no WPR is operated. In this study, meteorological Doppler radar data were added to the wind profiler observation network for 3D wind field guidance, and the range of the 3D wind field was expanded. The Doppler radar data are recorded in the universal format, and the reflectivity, radial velocity, and spectral width are recorded according to the azimuth, distance, and altitude. They are processed by the data quality control algorithm of the Open System Radar Product Generator (ORPG) [21]. Radars have the same continuous operating mode based on a data collection cycle of 10 min duration. The cycle is composed of 10 to 15 plan position indicator scans at different elevations. The horizontal data acquisition is limited to a radial range of 250 km with data gates spaced by 200 m. The VVP method is used to retrieve the wind from vertical profiles of the radial velocity assuming horizontal linearity of the wind fields [22].

Recently, high-impact weather phenomena, such as severe rain storms, flash floods, and heavy snow, have been increasing in frequency. Global and regional forecasting models are limited in accuracy to predict the generation, intensity, and spatiotemporal evolution of these exceptional events. The KMA operates a numerical weather forecasting system for short and medium-range forecasting

that combines a global model, two regional models, a local model, and various application and statistical models. The KMA global model, which is based on the Unified Model (UM) from the United Kingdom Met Office is the core of the forecasting system, predicting weather for the entire globe with no boundary conditions. The regional models carry out predictions using boundary conditions from this global model. The regional models for East Asia include UM 12-km L70 (UM with 12 km horizontal resolution and 70 vertical levels) and the Korea Weather Research and Forecasting with 10-km horizontal resolution. The KMA has set up a 1.5 km resolution model called the Local Data Assimilation and Prediction System (LDAPS) to predict high-impact weather phenomena in and around the Korean peninsula [23–25]. LDAPS focuses on individual storm forecasting until 1–3 h before the event and improves the forecasting of rainfall, strong winds, etc. until 24 h before the event. In this study, the wind vector fields retrieved from the network of wind profilers will be compared to those analyzed by LDAPS at the UHF profiler site (see Figure 2).

Each wind profiler was collocated with a ground-based microwave radiometer that measures the downwelling radiance in the form of brightness temperature in the microwave region (Table 2), and it creates a vertical profile of humidity as well as air temperature. These radiometers operated by KMA were installed for nowcasting and for utilization by numerical weather prediction models to complement the wind profilers observations [26]. High temporal resolution data from radiometers can resolve the changing thermodynamic structure of transitioning boundaries, including fronts and gravity waves. A significant potential benefit of radiometers is that they can detect thermodynamic changes on very short time scales, on the order of approximately 10 min, which is far too short to be captured by radiosondes [26]. We used vertical thermodynamic information provided by radiometers and radiosondes to produce CAPE.

Table 2. Observation periods and data.

Site		Period	Lat (° N)	Lon (° E)	Data
P1	Changwon	2013.06.17–2013.06.20	35.18	128.58	Wind profiler, Radiometer, LDAPS
P2	Gunsan	2013.06.17–2013.06.20	36.01	126.77	Wind profiler, Radiometer, LDAPS
P3	Chupungnyeong	2013.06.17–2013.06.20	36.23	128.00	Wind profiler, Radiometer, LDAPS
P4	Uljin	2013.06.17–2013.06.20	37.00	129.42	Wind profiler, LDAPS
P5	Wonju	2013.06.17–2013.06.20	37.34	127.95	Wind profiler, Radiometer, LDAPS
P6	Gangneung	2013.06.17–2013.06.20	37.81	128.86	Wind profiler, LDAPS
P7	Munsan	2012.10.26–2012.10.27 2013.06.17–2013.06.20	37.89	127.77	Wind profiler, LDAPS
P8	Cherwon	2013.06.17–2013.06.20	38.15	127.31	Wind profiler, LDAPS
W1	Jindo	2013.06.17–2013.06.20	34.47	126.32	Doppler Radar, LDAPS
W2	Gosan	2013.06.17–2013.06.20	33.29	126.16	Doppler Radar, LDAPS
W3	Seongsan	2013.06.17–2013.06.20	33.39	126.88	Doppler Radar, LDAPS
W4	Kwanaksan	2012.10.26–2012.10.27	37.44	126.96	Doppler Radar, LDAPS

2.2. *Analysis Method*

2.2.1. Three-Dimensional Wind Field Processing

The 3D wind vector fields were deduced from the measurements made by the triangle network of UHF profilers. The technique to retrieve the 3D atmospheric field from the wind profiler network observations is based on the assumption of linearity of the fields inside a limited spatial and temporal domain. A field of a quantity X measured by the radars, as a function of latitude x, longitude y, altitude z, and time t, is represented by the following Taylor series limited to the linear terms:

$$X(t_0 + \Delta t, x_0 + \Delta x, y_0 + \Delta y, z_0 + \Delta z) = X(t_0, x_0, y_0, z_0) + \Delta t \frac{\partial X}{\partial t} + \Delta x \frac{\partial X}{\partial x} + \Delta y \frac{\partial X}{\partial y} + \Delta z \frac{\partial X}{\partial z} + \zeta \quad (1)$$

where (t_0, x_0, y_0, z_0) is a reference point and ζ is the departure from the linear model. For a time t_0 and an altitude z_0, the coefficients of the series are extracted through a weighted least squares fitting over all wind profiler data $X(t, x, y, z)$ that satisfies $t0 - \Delta t/2 < t < t_0 + \Delta t/2$ and $z_0 - \Delta h/2 < z < z_0 + \Delta h/2$.

The parameters Δt and Δh have a decisive effect on the time and height resolution, attenuation of data noise, and spurious echo removal [20]. In the triangle consisting of P1, P2, and P3, P0 is the reference point with Δt of 60 min and Δh of 250 m. The horizontal resolution of the technique is a direct function of the mean size of the profiler triangle, i.e., around 100 km. The fitting equation is solved in two steps; the first pass is used to remove data that are too far away from the linear model. Usually, less than 5% of the data are removed. Vertical profiles of (X_0, $\partial X/\partial t$, $\partial X/\partial x$, $\partial X/\partial y$, $\partial X/\partial z$) functions of time and height, are obtained when varying t_0 and z_0.

The 3D wind field allows determination of the Lagrangian trajectory at any point and time of the domain, as the trajectory requires that wind speed be a function of time and distance [19]. White et al. [27] showed the advantage of profiler-based trajectories from the NOAA wind profiler 3D network, which provided descriptions of weather patterns at finer time scales than those of operational upper-air balloon soundings. The movement trajectory of an air mass with time can be calculated using the constant acceleration solution.

$$X_1 = X_0 + \left(\frac{dX_0}{dt} + \frac{dX_1}{dt}\right)\frac{\Delta t}{2} \tag{2}$$

where X_0 is the position of the air mass at time t_0 and X_1 at t_1 (= t_0 + Δt). The air mass velocity $\frac{dX_1}{dt}$ from the wind profiler network is repeatedly applied to Equation (2). This trajectory is compared with the radiosonde trajectory and used as a means for quantitative verification. The rising velocity of the air mass and balloon was not considered and the horizontal movement trajectory of the air mass was calculated with the altitude of the radiosonde.

2.2.2. Convective Instability Indices

A layer of air in which the air-parcel motion is stable with respect to saturated, vertical displacements can become conditionally unstable when the entire layer is lifted to saturation. Many indices have been introduced to evaluate the state of the atmosphere, specifically for convective and severe weather potential, which combines measures of the thermal and moisture properties, and the wind shear of the lower atmosphere. One such index, CAPE, has become very popular as a method for evaluating the convective potential of the atmosphere. In contrast to single-level stability indices, CAPE is a vertically integrated index that measures the cumulative buoyant energy in the free convective layer from the level of free convection (the level at which the parcel temperature exceeds the ambient temperature and at which parcels are unstable relative to their environment) to the equilibrium level [28]. The formal definition is given by:

$$\text{CAPE} = g\int_{LFC}^{EL} \frac{T_v(z) - \overline{T_v}(z)}{\overline{T_v}(z)} dz \tag{3}$$

where T_v is the virtual temperature of the parcel, $\overline{T_v}$ is the virtual temperature of the environment, EL is the height of the equilibrium level, LFC is the level of free convection, and g is gravity [29]. The computed value of CAPE can vary significantly depending on the choice of parcel. As the cumulative experience in both the operational and research environment grows, certain behavioral characteristics of CAPE have become apparent and need to be fully understood to take advantage of the information contained within this index [28].

The storm relative helicity (SRH) is used to estimate dynamic instability, which investigates the influence of convective storm structure and evolution, with a particular emphasis on the identification of ambient shear profiles conducive to the development of long-lived, strongly rotating storms [30]. The SRH is calculated by multiplying the storm-relative inflow velocity vector by the stream-wise vorticity and integrating this quantity over the inflow depth. Geometrically, the storm-relative environmental helicity is represented by the area on a hodograph swept out by the storm-relative

wind vectors between specified levels, which is typically the surface and 3 km to represent the primary storm inflow [31,32]. It is regarded as a measure of the rotation tendency of a supercell. The formal definition is given by:

$$SRH = \int_{0\ km}^{3\ km} \left(\nabla \times \vec{V_H}\right) \cdot \left(\vec{V_H} - \vec{V_C}\right) dz \tag{4}$$

where $\vec{V_H}$ is the horizontal velocity vector and $\vec{V_C}$ is the storm motion vector. The low-level SRH is a good indicator of the potential for tornadoes and can be an important prognostic variable for severe weather forecasting [33–36]. Thus, it is important to obtain accurate estimates of the low-level SRH, which is known to have significant spatial and temporal variations [32,34]. Because soundings are infrequent and are only meant to capture the synoptic-scale environment, the WPR3D is adequate to resolve the front-scale variability of SRH. Richardson et al. [37] found that heterogeneities within the mesoscale environment can also be important, at least in numerical simulations. These mesoscale heterogeneities would not be captured by sparse and infrequent soundings [38].

2.2.3. Accuracy Validation

Comparisons of WPR3D and either LDAPS or single wind profilers were conducted to evaluate the accuracy and quality of the wind profiler observations. The accuracy of the wind profiler at each site was investigated and used as a basis for finding the cause of error. The accuracy of a wind profiler was calculated with the skill scores in Table 3. V_W and V_L are the wind vectors of the wind profiler and LDAPS, respectively. $\overline{L}$ and $\overline{W}$ are the mean values for V_W and V_L; the root mean square error (RMSE) is the absolute magnitude of the wind profiler error. The accuracy (ACC) is the remainder for the average wind vector of the radiosonde in the percentage of RMSE. The N in Table 3 represents the number of wind profiler and LDAPS data points for each altitude. The mean bias (MB) is related to the wind profiler error. If the mean deviation sign is positive, it means that the wind profiler is overestimating compared to LDAPS.

Table 3. Skill scores for accuracy validation of wind vectors.

Skill Score	Symbol	Statistic Definition	Unit
Mean Wind Profiler	$\overline{W}$	$\frac{1}{N}\sum_{i=1}^{N} V_W$	m s^{-1}
Mean LDAPS	$\overline{L}$	$\frac{1}{N}\sum_{i=1}^{N} V_L$	m s^{-1}
Mean Bias	MB	$\frac{1}{N}\sum_{i=1}^{N} (V_W - V_L)$	m s^{-1}
Root Mean Square Error	RMSE	$\sqrt{\frac{1}{N}\sum_{i=1}^{N} (V_W - V_L)^2}$	m s^{-1}
Correlation Coefficient	CORR	$\frac{\sum_{i=1}^{N}(V_W-\overline{W})(V_L-\overline{L})}{\sqrt{\sum_{i=1}^{N}(V_W-\overline{W})^2}\sqrt{\sum_{i=1}^{N}(V_L-\overline{L})^2}}$	
Accuracy	ACC	$100 - \left(\frac{RMSE}{\overline{L}} \times 100\right)$	%

V_W: Measured by wind profiler radar, V_R: Measured by radiosonde.

In the comparison of the WPR3D and a single profiler, non-averaged data were taken at 71 equivalent height points. Therefore, the total number of comparison points should be 30,672 for three days at 71 heights. We used a threshold of 3σ to reject points that differed by too much. The data collection rate is reduced above 3 km, so the number of comparison pairs is about 20,000. In the comparison of WPR3D and LDAPS, we used 10 vertical layers up to 5 km of the LDAPS that had been set up at 1.5 km × 1.5 km horizontal resolution. We took the four closest horizontal grid points of the LDAPS from the WPR reference site, so the number of comparison pairs is about 900 for three days at 10 heights. Since the WPR's oblique beam measures the atmosphere about 1 km away from the vertical

beam above 3 km altitude, four separate points were individually compared with the WPR at the triangle center P0. As a result, increased comparison pairs are expected to improve statistical reliability.

3. Results and Discussion

3.1. Synoptic Conditions and Frontal Structure

During June 2013, as the force of the North Pacific high pressure expanded, the Jangma front formed over the northern part of the Korean peninsula (Figure 3). A squall line occurred near 40° N around 00 UTC 17 June 2013 and moved southward to 37° N at 12 UTC 17 June. Then, at 12 UTC 18 June, the low pressure on the squall line moved eastward along a latitude of 37° N, forming a long-lasting east–west squall line. Due to a weakening of the North Pacific high pressure, the squall line that was previously stationary at 37° N moved south to 34° N between 12 UTC 18 June and 12 UTC 19 June.

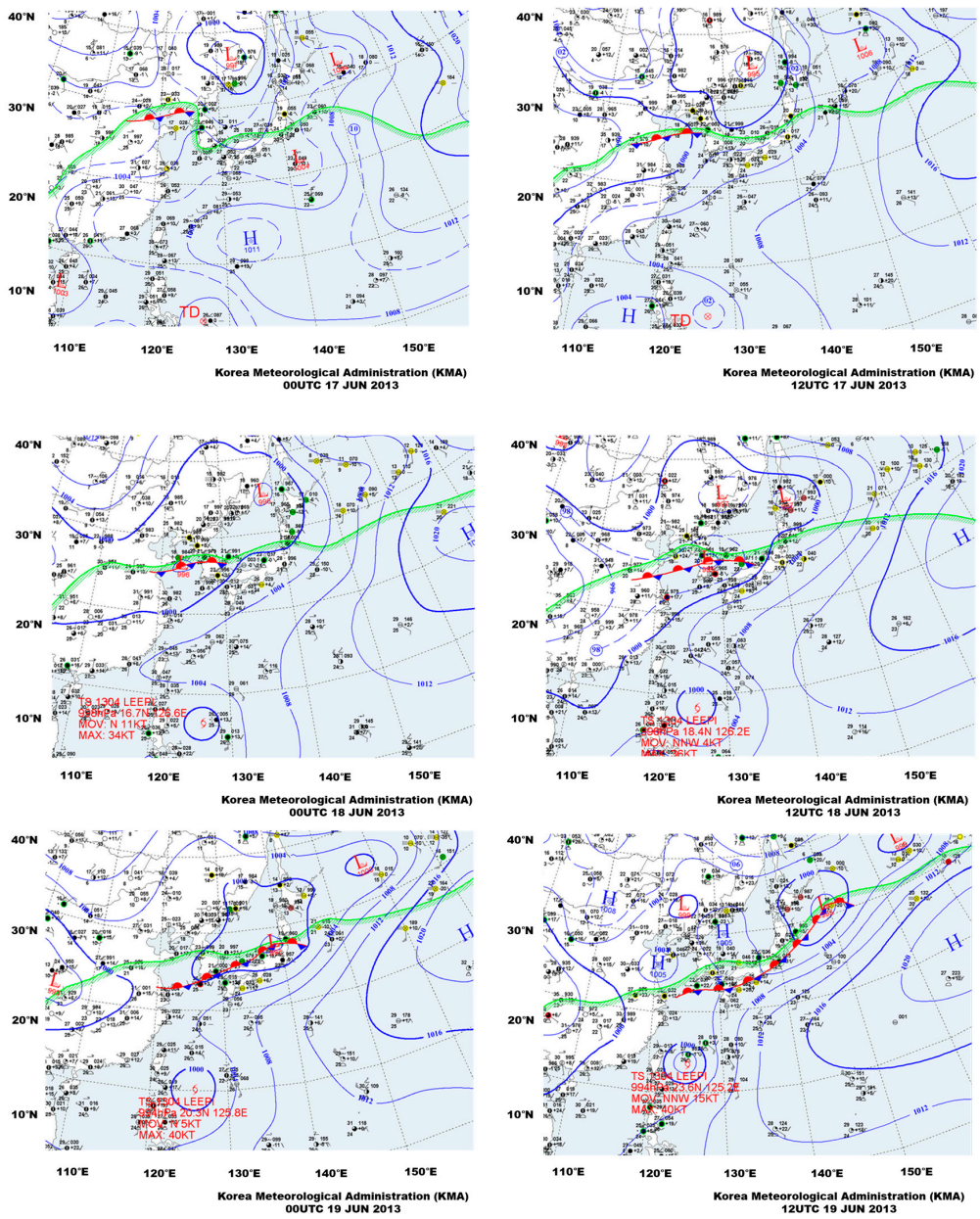

Figure 3. Surface weather maps show Jangma front movement. The green line and the hatched zone indicate the area where the dew point temperature is 20 °C or higher.

While the southward movement of the squall line occurs, there is a high probability of heavy rains due to the frontal structure where the dry and cold air in the north push up the warm and wet air. During the precipitation period, the squall line passed through the wind profiler sites of P0, P1, and P3 (Figure 4). The wind profiler observations show that the front moved from north to south and the frontal boundary became steeper. As the front passed, the surface wind direction changed abruptly in a clockwise direction from eastward to southward winds. After the front had passed, the wind direction changed counterclockwise further eastward winds with increasing altitude. The wind speed also decreased drastically with decreasing altitude, and the wind speed within approximately 2 km of the surface was generally below 5 m s^{-1}. The Jangma front approached P1 and P0 from the north at 15 UTC on June 18 and passed the southernmost site, P3, at 21 UTC on June 18. The temporal variation of the observed winds coincided with the movement of the front shown in the weather chart in Figure 3. The WPR detected smaller phenomena in scale than what White et al. [27] observed. They noted that changes in wind direction in the lower troposphere that occurred with the passing synoptic features are clearly indicated early in the observed wind profiler data.

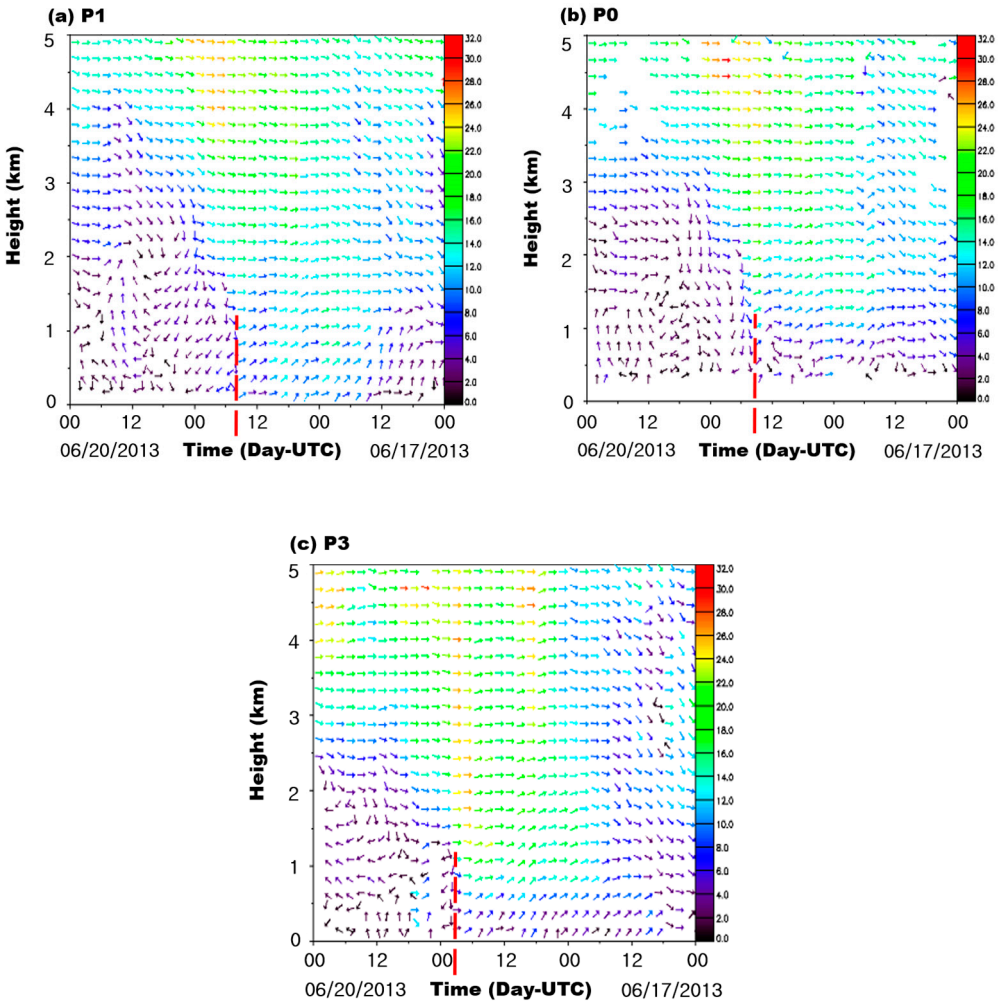

Figure 4. Wind vectors observed by wind profilers (**a**) at P1, (**b**) at P0, and (**c**) at P3 with an inverse time axis. Red dashed lines indicate the arrival of front at each site.

Heavy rain occurred along the path of the Jangma front. This front moved southward, and a squall line over 400 km long formed in an east–west direction on the south coast of the Korean peninsula at about 00 UTC 19 June 2013 (Figure 5). Precipitation was recorded at each wind profiler site, tracking the movement of the squall line (Figure 6). The rain started at 12 UTC 17 June at P1 and measured

up to 15 mm h^{-1} at 03 UTC 18 June. Rainfall was detected at P0 from 20 UTC 17 June and there was heavy precipitation of 27 mm h^{-1} and 15 mm h^{-1} at 00 UTC and 09 UTC 18 June, respectively. The rain began at 09 UTC 18 June, and 18 mmh^{-1} of precipitation was recorded before 12 UTC at P3. Heavy precipitation of up to 15–25 mm h^{-1} was measured from 15 UTC at this site.

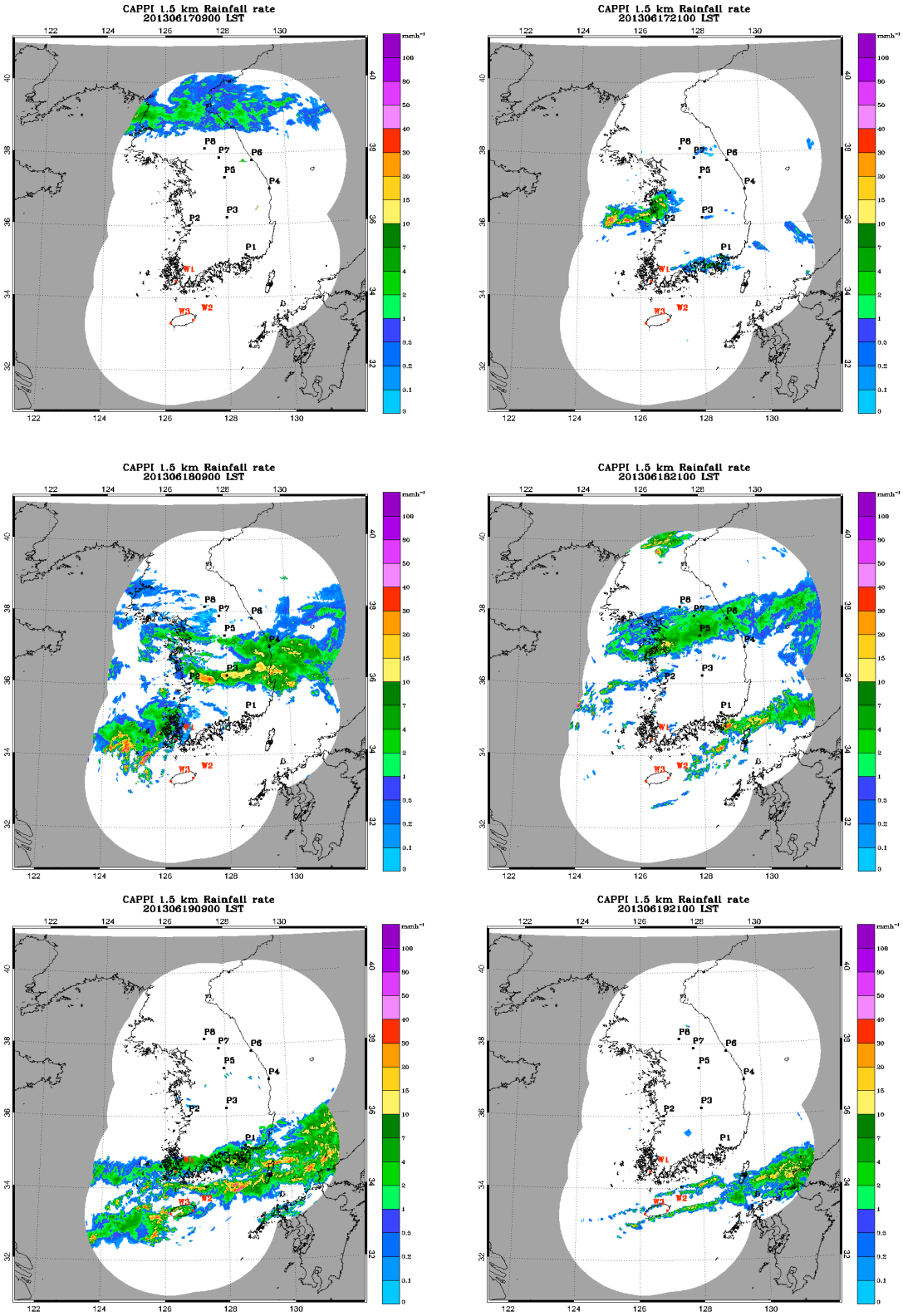

Figure 5. Composed radar images during Jangma front migration.

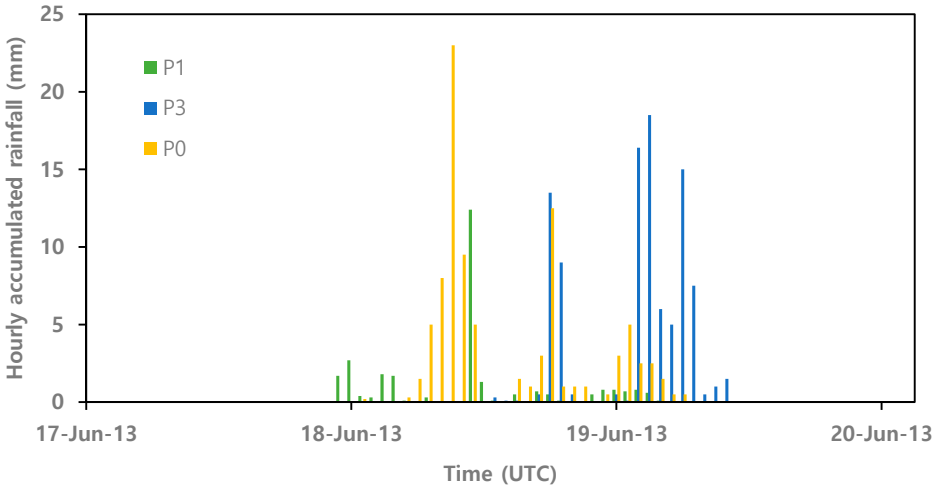

Figure 6. One hour accumulated rainfall from 17 to 20 June 2013 at P0, P1, and P3.

3.2. Assessment of Frontal Winds from a Single WPR3D

In order to analyze the quantitative accuracy of WPR3D using statistical methods, the wind magnitude and wind direction observed at P0 and the LDAPS wind field were used as reference values from 00 UTC 17 June to 00 UTC 20 June 2013 in Figure 7. The color index at the right side of each graph is the frequency of the compared data pairs. High frequencies in red, yellow, and green are found on the equivalent line, which show the WPR3D wind vector being in good agreement with that of both the single wind profiler radar (WPR) at P0 and the LDAPS. Statistical accuracy parameters such as the CC (correlation coefficient), RMSE, MB, and ACC were estimated, as shown in Figure 7. The maximum wind speed measured by the wind profiler was 29 m s^{-1}, and weak wind speeds less than 5 m s^{-1} were dominant at all altitudes. The wind speed of WPR3D based on P1, P2, and P3 showed a relatively good correlation (~0.6–0.89) with that from the single WPR at P0. The WPR3D wind speed was in good agreement with the wind profiler wind speed between 10 m s^{-1} and 20 m s^{-1} that dominate at all heights. The RMSE of the U component and V component between WPR3D and the wind profiler at P0 was 3.39 m s^{-1} and 2.58 m s^{-1}, respectively, and the RMSE of their wind speed was 3.16 m s^{-1}. The MBs of the U and V components were −0.48 m s^{-1}, −0.04 m s^{-1}, respectively and the MB of the wind speed was −0.64 m s^{-1}. Although the WPR3D wind slightly underestimated the WPR at P0, the ACC of WPR3D was as high as 70.02%. The WPR3D wind vector was in good agreement with the LDAPS wind vector for P0 (Figure 7b). The correlation coefficients of the U and V components were 0.89 and 0.60, respectively, and the wind speed was 0.87. The RMSEs of the U and V components were 3.31 m s^{-1} and 3.06 m s^{-1}, respectively, and the wind speed was 3.28 m s^{-1}. The MBs were −1.46 m s^{-1}, −1.57 m s^{-1}, and −1.42 m s^{-1}, respectively. Although the WPD3D wind speed was underestimated compared to the wind speed determined from LDAPS, the ACC of WPR3D was as high as 71.5%. Comparisons with sounding data at 7 sites except P0 were performed at different times [39]. The wind speed showed a similar correlation (~0.65–0.85 with that from the single WPR at 7 sites. The MB of the wind speed was approximately −1.2 m s^{-1} to 0.3 m s^{-1}, and the RMSE ranged from 1.2 m s^{-1} to 2.9 m s^{-1}. Therefore, it is implied that the WPR3D is as useful as the single profiler.

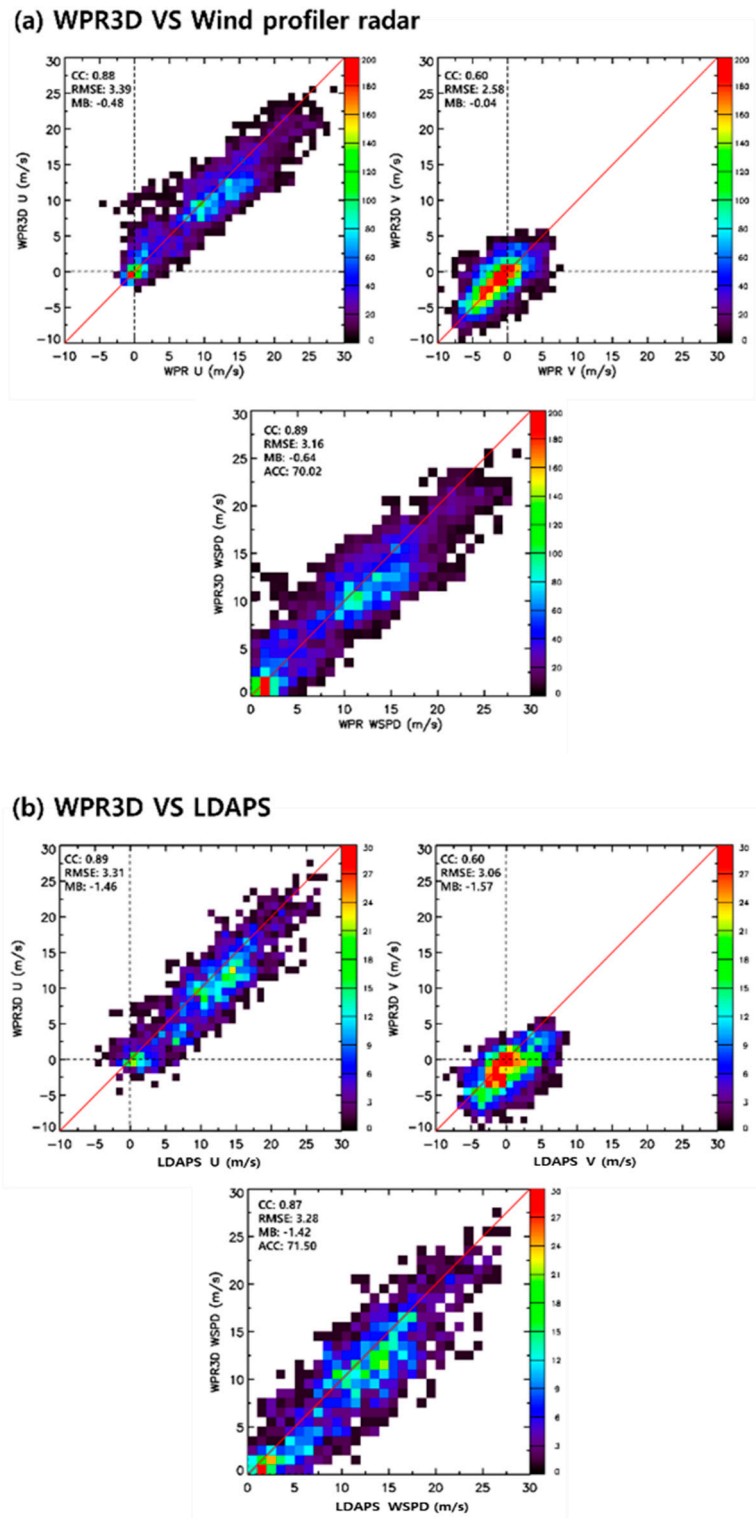

Figure 7. Comparison of wind components U, V, and WPR3D wind speed with those (**a**) from WPR at P0, and (**b**) from Local Data Assimilation and Prediction System (LDAPS) around P0 at an altitude of 1.5 km.

Figure 8 shows the accuracy of the WPR3D wind speed compared to the LDAPS wind speed as well as to the wind profiler with height at P0. The CC increased by 0.8 over 1 km and was highest at ~1–2.5 km. The RMSE was less than 3 m s^{-1} below 1.5 km and less than 3.5 m s^{-1} up to 5 km. The MB was less than −2.0 m s^{-1} at all altitudes, and the wind speed of WPR3D was slightly underestimated.

The accuracy of the WPR3D increased to 80% over 3 km altitude. The CC of WPR3D compared to the wind speed of LDAPS was as high as 0.75 or more between 0.75 km and 5 km altitude. The RMSE was higher than 4 m s^{-1} at a height of ~0.75–1.5 km, but it decreased to below 3 m s^{-1} as the altitude increased above 1.5 km. The MB was less than −2 m s^{-1} up to 2 km and less than −1 m s^{-1} above that altitude. The accuracy of the WPR3D compared to the mean wind speed of LDAPS increased with altitude and showed a good agreement of more than 60% above 2 km. The accuracy of WPR3D compared to the wind speed of LDAPS was lower than the single wind profiler at P0 since the LDAPS simulated stronger wind speeds than the wind profiler did below 2 km. As a result, the RMSE of WPR3D versus LDAPS was high for the weak wind speed in the lower layer. Wind profiler data also are susceptible to contamination by surrounding terrain clutters, which can lead to RMSE values being higher as the spatiotemporal variability of the wind vector is affected by the surface [17].

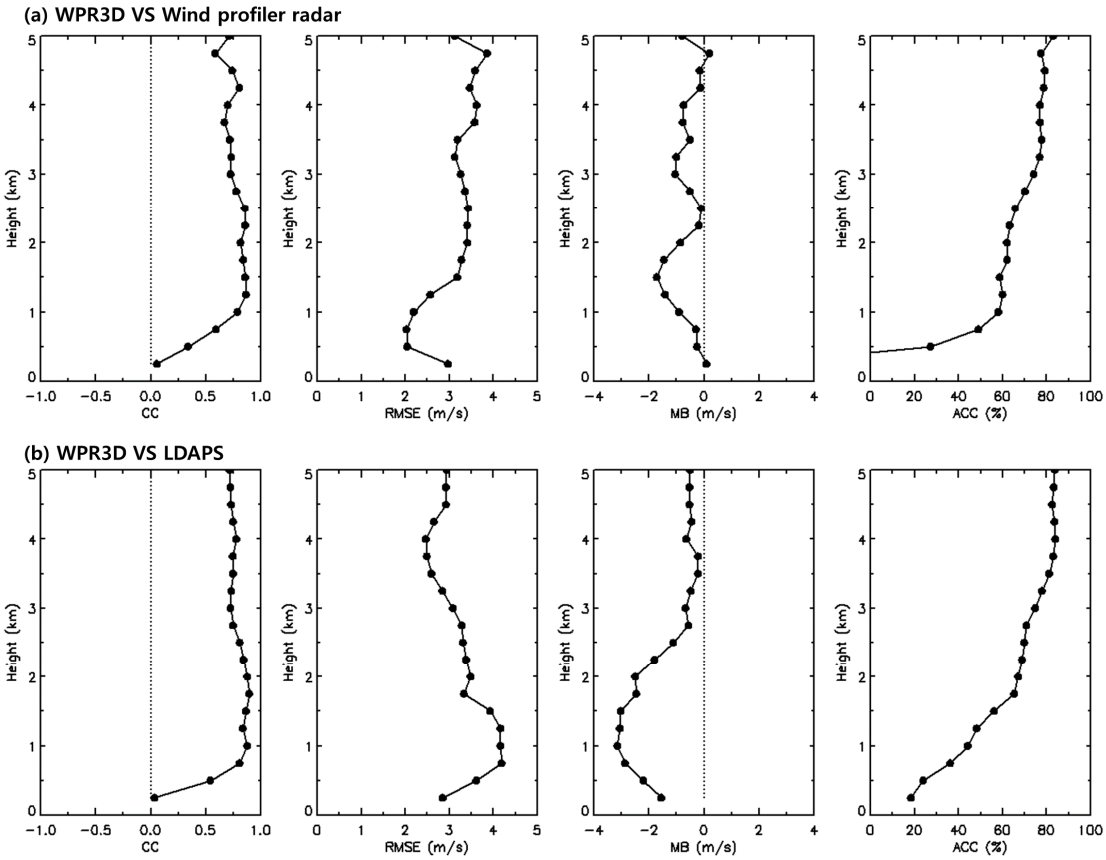

Figure 8. Skill scores with height used for validating the wind determined from WPR3D against the wind (**a**) from the single wind profiler at P0 and (**b**) from LDAPS.

3.3. Instability and Wind Field

SRH and CAPE were calculated using wind profiler data and radiometer data for thermodynamic analysis of the front. Figure 9 shows that the intensity and duration of precipitation were significantly correlated with SRH. During the non-precipitation periods, SRH was mostly less than 150 m^2 s^{-2}. After precipitation of over 15 mm h^{-1} for ~1–3 h, SRH was 300 m^2 s^{-2} or more. CAPE was less than about 200 J kg^{-1} before the passage of the squall line and was almost 0 J kg^{-1} during the precipitation that continued with the passage of the squall line (Figure 10). Therefore, it is considered that the squall lines generated by the Jangma front developed via dynamic instability rather than by thermal convective instability.

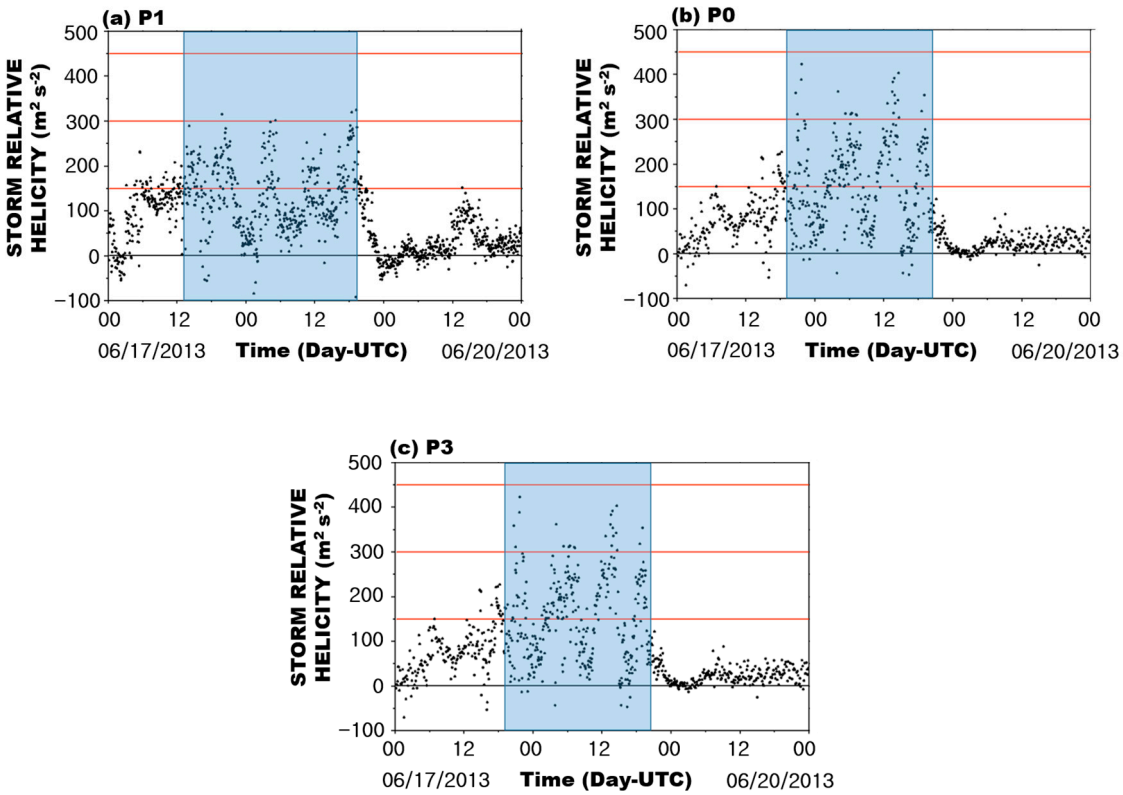

Figure 9. Storm relative helicity (SRH) produced from wind profiler observations (**a**) at P1, (**b**) at P0, and (**c**) at P3. The rainfall period is shaded in blue.

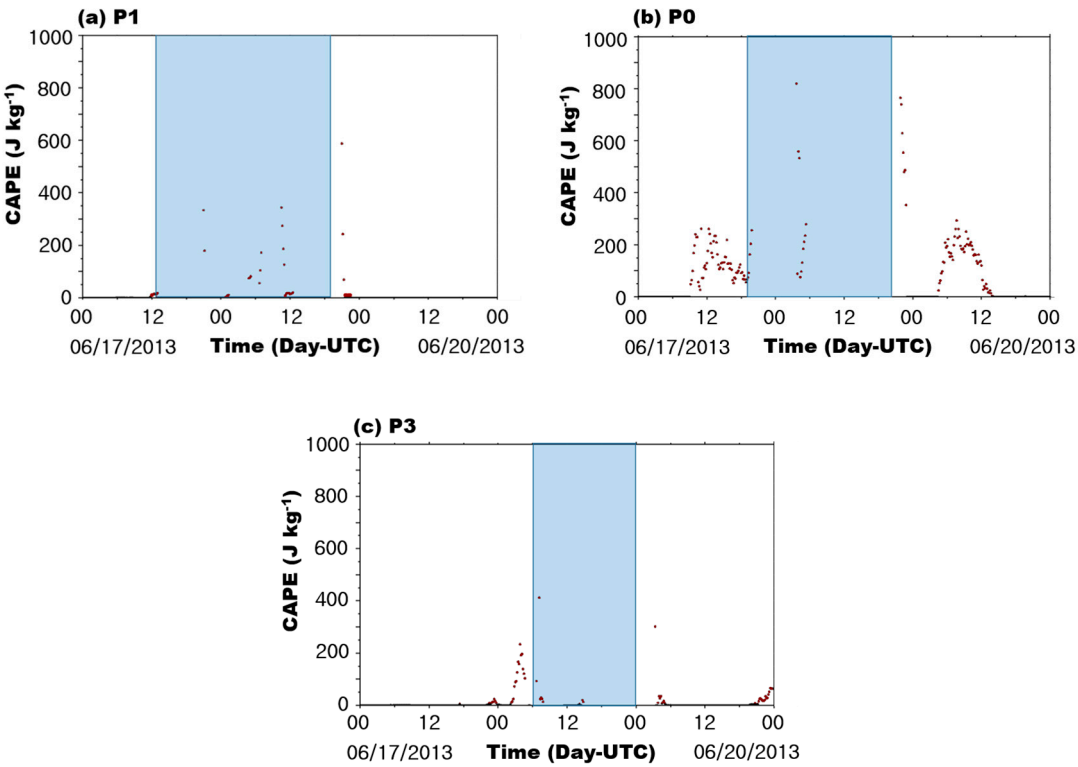

Figure 10. Same as Figure 8 but for convective available potential energy (CAPE) (**a**) at P1, (**b**) at P0, and (**c**) at P3.

The wind vectors were calculated at the reference point P0 of WPR3D, and their distribution shows the structure of the Jangma front (Figure 11a). From 15 June onward, surface winds rapidly changed from an eastward to a southward direction, and after 18 UTC on 17 June, they changed from a northward to an eastward direction with increasing altitude. Also, after the front passed through, the wind veered, and the wind speed decreased sharply below 5 m s^{-1} within 2 km from the surface. This result shows a good agreement with the horizontal wind structure in the time–height plane retrieved from the wind profiler at P0 (Figure 4b). Compared to the wind field measured at P0 (Figure 4b, a gap-filling effect was also found at around 4 km altitude at 00 UTC on 17 June and from 12 UTC on 19 June to 00 UTC on 20 June. The front, as seen via the LDAPS wind fields, had a similar wind speed after frontal passage as that observed at P0 (Figure 4b).

In WPR3D, SRH was calculated using the wind vector at P0 (Figure 12a). During the period of precipitation, the SRH was 150–250 m^2 s^{-2}, which explains the dynamic instability of the squall line, although it was underestimated compared to that of the single WPR at P0. Intense precipitation of more than 15 mm h^{-1} occurred in the three hours after the SRH over 200 m^2 s^{-2}. This was consistent with the SRH variation pattern obtained from the single WPR at P0. It is possible, therefore, to predict storm occurrence using WPR3D. The SRH calculated by the horizontal wind vector of the LDAPS at P0 was approximately ~150–300 m^2 s^{-2} during the period of precipitation, which indicated strong dynamic instability of the squall line (Figure 12b). However, the variation range of the SRH was larger in LDAPS than in WPR3D. When precipitation of 15 mm h^{-1} or more occurred, the SRH was high too. The high temporal resolution of WPR3D can be more effective to diagnose the continuous variability of SRH.

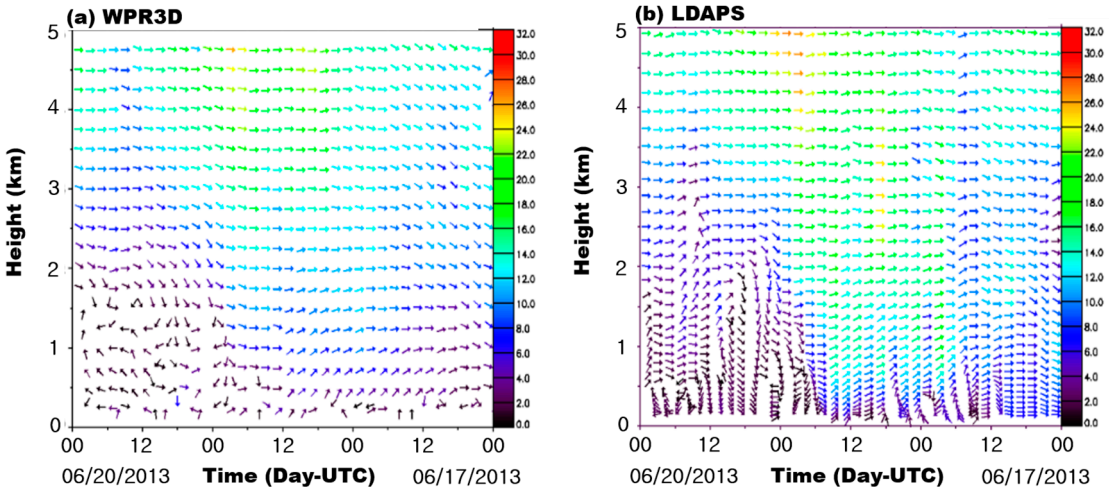

Figure 11. Wind vectors (**a**) from WPR3D and (**b**) from LDAPS at the P0 station.

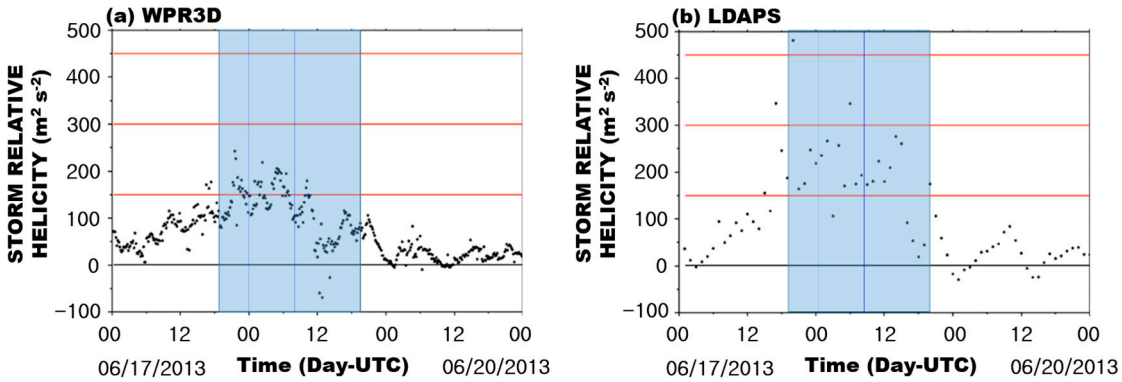

Figure 12. SRH (**a**) from WPR3D and (**b**) from LDAPS. The blue shading indicates the rainfall period with rainfall over 15 mm h^{-1}.

3.4. Multiple WPR3D Wind Field

In order to determine whether the WPR3D simulated dynamic variation due to the front, we investigated the wind field from the single WPR3D and the LDAPS with a horizontal resolution of 10 km at an altitude of 1.5 km and within a radius of 50 km around P0 (Figure 13). The LDAPS wind field was analyzed every 3 h from 15 UTC 18 June to 00 UTC 19 June. The WPR3D produced a strong eastward wind of more than 10 m s^{-1} at 15 UTC 18 June when the Jangma front began to pass through site P0. These results were not similar to the southwestern wind direction obtained from LDAPS, which was affected by LLJ. From 15 UTC to 21 UTC 18 June, the WPR3D wind shifted from an eastward to a southeastward wind, and the wind speed gradually decreased. On 19 June at 00 UTC, the wind direction changed to southward winds with the passing of the Jangma front near P0, which coincides with the LDAPS wind fields. However, on 19 June at 00 UTC, the wind field southwest of P0 differed significantly from the nonlinear wind field of LDAPS. Because the WPR3D wind field algorithm using the wind profiler network is based on the linearity of the wind, it is possible that the nonlinear wind is not correctly realized. In addition, discrepancies in the southwestern region of P0 are due to a lack of data in the southwestern region and to the southwestern mountainous terrain of P0 (see Figure 2). The HyMeX showed how the various combinations of radars behave for specific wind patterns and different degrees of heterogeneity over the northwestern Mediterranean basin [20]. Wind fields retrieved by the network were compared with AROME-WMED (Application of Research to Operations at Mesoscale-West Mediterranean Sea) model analysis fields. As the wind observed at the Pianottoli site, which is located in the southwestern region, is almost null, the large network was not able to retrieve the correct flow at a larger scale. In addition, Saïd et al. [20] emphasized the requirement of another wind profiler radar (Levant radar) on the southwestern edge of the domain to capture the dominance of Mistral. The Levant radar is important to impose a constraint at the eastern part of the Mistral plume. When the Levant radar is not included, the network fails to constrain the eastern part of Mistral plume. In Figure 13, a curvature of the gyre is not retrieved by the WPR3D at 00 UTC 19 June on the southwestern region where there are no wind profilers operating.

For observational gap-filling, S-band Doppler radar is an alternative to WPRs. We improved the uncertainty of the wind field in the empty southwestern region of the wind profiler network. Three meteorological S-band Doppler radars (W1, W2, and W3) were added to the wind profiler observation network creating the multiple WPR3D network (M-WPR3D) (Figure 2). The Taylor series solution for the expansion of the 3D wind field was derived from R1 to R11, and the retrieved wind field was synthesized on the Korean peninsula scale. The VVP technique was used to deduce the wind field from the S-band radar on the assumption of horizontal and vertical linearity. This assumption was supposed to be fulfilled in horizontal cylindrical slices of 250 m depth and within a radial distance of 75 km. The same assumption of linearity of the field was also used for the triangle formed by three profilers for cylindrical slices of 200-m depth. On 17 and 18 June 2013, Kim et al. [40] compared the wind velocity deduced from the S-band weather radar KWK (Kwanaksan radar) located at W4 between P4 and R5 (50 km from P4) with that from the triangle of UHF profilers (P1–P2–P4). The wind vector from S-band Doppler radar in the vicinity of the reference point R5 was in a good agreement with that of the single WPR3D [40,41]. In order to examine the usefulness of the radar wind field, we selected a case in which the wind was relatively strong and the changes in wind direction and wind speed could be visualized. Figure 14 shows wind fields based on the S-band radar near R5 and the single WPR at P4. The wind directions are almost identical although the wind speeds are slightly different in the weak wind zone. These results allow the S-band Doppler radar to play a role with the wind profiler for the M-WPR3D.

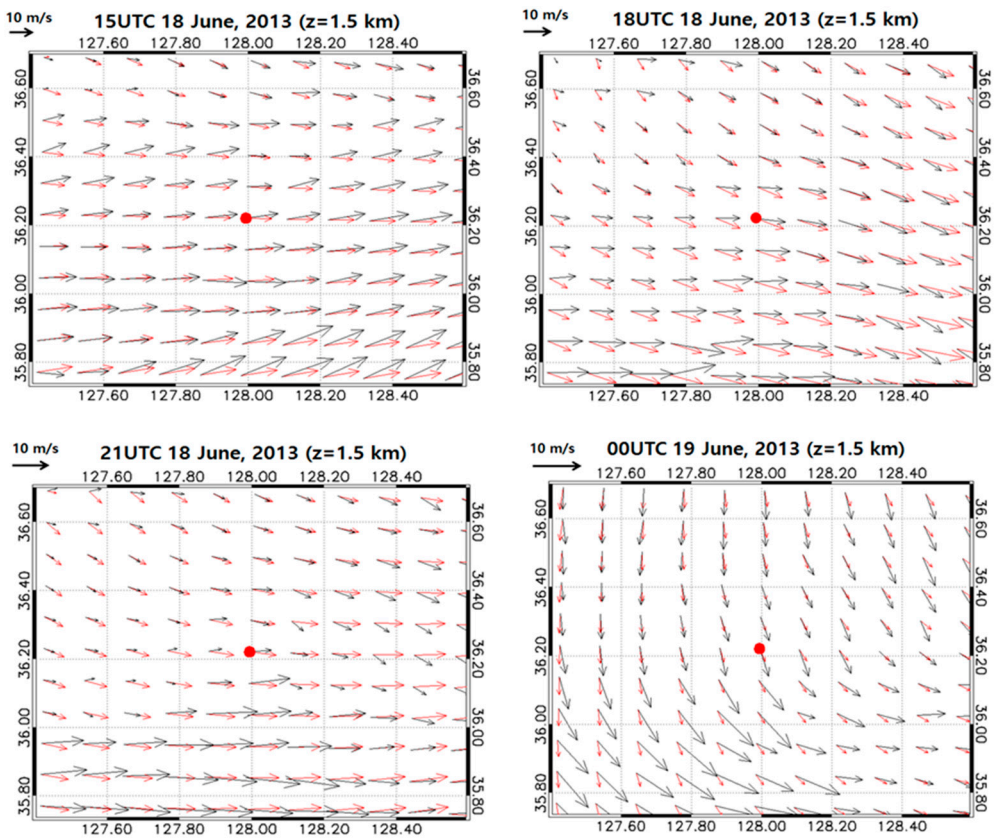

Figure 13. Wind vector from WPR3D (red) and LDAPS (black) at the 1.5-km level. P0 is shown by the red point in the center.

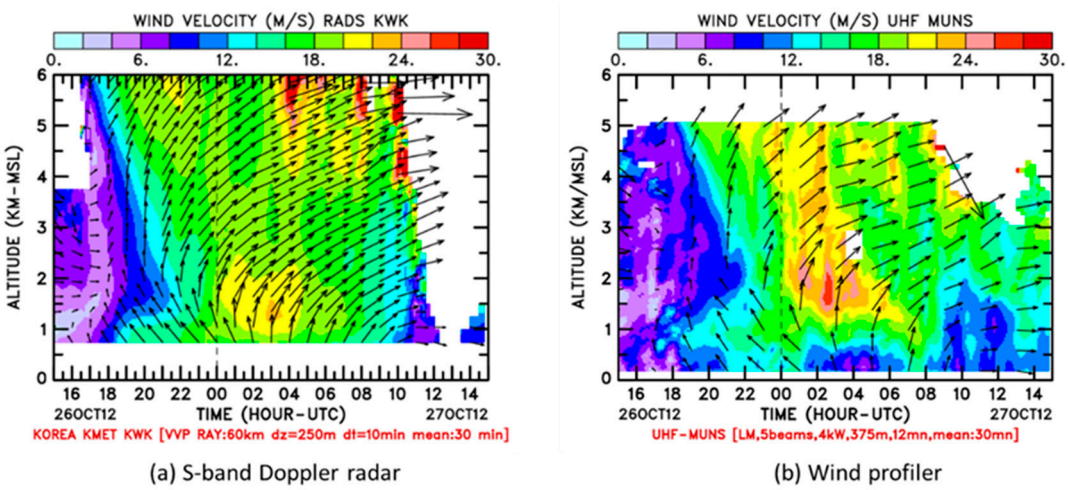

Figure 14. Comparison of the horizontal wind fields (**a**) from the S-band radar near R5 with those (**b**) from the WPR at P4 on 26–27 October 2013.

For the purpose of validating the M-WPR3D, trajectories of the radiosonde launched at P1 and P6 were compared with air mass trajectories calculated from M-WPR3D. The trajectory of the radiosonde expressed the effect of the frontal wind resulting from the movement of the Jangma front well. As shown in Figure 15a, the radiosonde moved about 20 km from P1 to the east by a strong wind resulting from an LLJ at 15 UTC on 18 June 2013 (see Figure 4a). As the Jangma front passed through P1, the wind vector changed into a weak southward wind at 23 UTC on 18 June 2013. The radiosonde moved a short distance of about 15 km southward by a weak southward wind. The air trajectory calculated from

M-WPR3D was very similar to the radiosonde trajectory. In particular, the features of the radiosonde trajectory before and after the Jangma front passed the launching point were reflected well in the air trajectory. The Jangma front passed through P6 before it passed through P1. The radiosonde launched at P6 moved a short distance within 10 km southward due to the influence of the Jangma front that passed through P6 at 15 UTC on June and continued to move until 23 UTC on 18 June 2013. The air trajectory calculated from M-WPR3D overlapped the radiosonde trajectory in Figure 14b. After the passage of the Jangma front, backing winds were shown on the radiosonde trajectory as well as on the air trajectory in Figure 15. Campistron et al. [19] reported there is an important spatiotemporal change in the wind, which induces a strong rotation on the trajectory of the radiosonde. The rotation is also observed in the M-WPR3D trajectory, but it is not so acute, and it occurs over a longer period of time. Saïd et al. [20] noted that the WPR network is able to capture the offshore wind acceleration over the Gulf of Lion during Mistral conditions and at levels ranging between 600 and 1300 m, but frequently underestimates the southward component of the Mistral. The WPR network overestimates the zonal acceleration outside the restricted area, because the linearity hypothesis no longer holds below a certain latitude depending on the characteristics of the low in the Gulf of Genoa, linked to the Mistral pattern. White et al. [27] calculated trajectories using a network of 10 wind profilers over a domain (approximately 320 km × 450 km). They showed profiler-based trajectories were more useful to describe the weather pattern than operational upper-air balloon soundings, and were therefore more accurate than the trajectories produced from numerical model initialization fields.

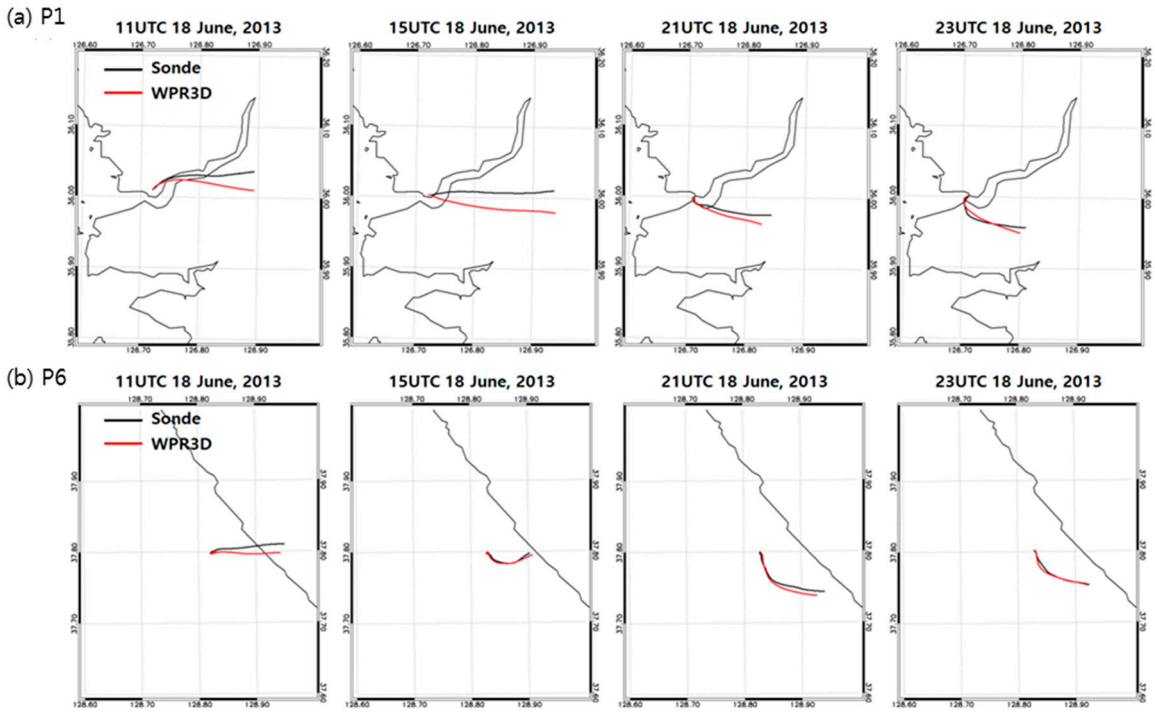

Figure 15. Comparison of the horizontal trajectories from M-WPR3D with those from the GPS radiosonde launched simultaneously (**a**) at P1 and (**b**) at P6 from 11 UTC to 23 UTC on 18 June 2013.

The wind vector from M-WPR3D shows the effect due to the LLJ over the southern region and the weak wind over the northern region in Figure 16. The M-WPR3D reflected the dynamic characteristics on the front and rear of the Jangma front. From 21 UTC 18 June to 00 UTC 19 June, the LLJ was retrieved in the southern part of 35° N. During this period, the M-WPR3D produced the dynamic characteristics on the rear as well as on the front of the squall line and realized backing wind vector in the west of P0. Since the wind direction is important for diagnosing temperature advection into the front, it is noted that the M-WPR3D with S-band radars may play a useful role in studying the front.

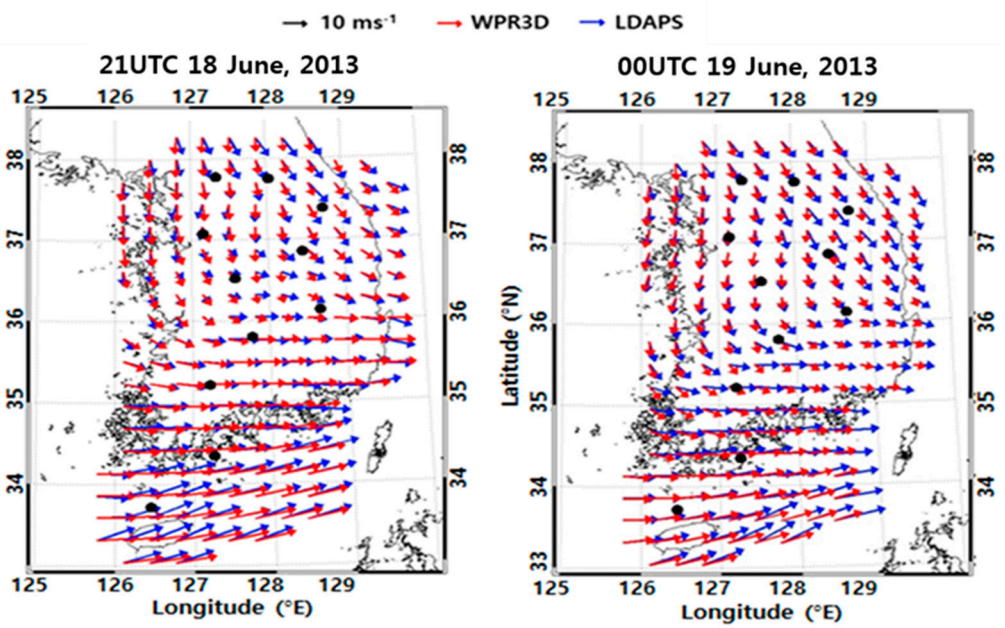

Figure 16. Comparison of the horizontal wind fields between the M-WPR3D (red arrow) and the LDAPS (blue arrow) at an altitude of 1.5 km.

4. Conclusions

Accurate observations of winds on the Jangma front are very important for understanding the complex dynamic interactions within MCSs over the Korean peninsula. The 3D wind field was reconstructed using the newly installed UHF WPR and S-band weather radar network data and the dynamical structure of the Jangma front was investigated. High spatiotemporal resolution wind data are used for short-term forecasting, model initial data embedded in a numerical model, and accurate recreation of the vertical structure of a meso-scale front. The accuracy of the WPR3D, examined using the single wind profiler and LDAPS wind vectors, was higher than 70% and increased with altitude. In the lower layer below 1 km, the accuracy was relatively low due to the ground clutter and a blind spot below 200 m. The WPR3D wind field showed a front structure moving from north to south. While the front passed through, the surface wind rapidly changed from eastward to southward winds. As the front moved southward, a squall line was formed, which resulted in heavy rainfall. The dynamic instability of the squall line was explained by the WPR3D. The SRH from WPR3D was repeatedly over 200 m^2 s^{-2} before heavy precipitation of over 15 mm h^{-1} began. This implies that storm events can be predicted based on a network of wind profilers. On the other hand, LDAPS did not correctly diagnose the sequential variability of the SRH. The retrieved wind field represented strong northeastward winds in the lower jet at an altitude of 1.5 km before the squall line passed; however, we found a difference between the WPR3D wind field and the LDAPS wind field near the boundary of the wind profiler network where the wind was backing. The VVP with three S-band weather radars created the M-WPR3D, which successfully retrieved the backing wind field in the rear of the Jangma front. The results of this study imply that the M-WPRD can provide real time detailed information on severe weather and local meteorological phenomena. M-WPR3D wind fields could be used as data for assimilation of numerical models to produce more accurate wind fields.

Author Contributions: Conceptualization, B.C.; methodology, B.C.; formal analysis, M.-S.K. and B.H.K.; validation, M.-S.K.; investigation, M.-S.K and B.H.K.; writing—original draft preparation, B.H.K.; writing—review and editing, M.-S.K. and B.H.K.; supervision, B.C. and B.H.K.; funding acquisition, B.H.K.

Funding: This work was supported by Civil-Military Technology Cooperation Program funded by the Korea Meteorological Administration and Defense Acquisition Program Administration. No. 17-CM-SS-23, KMA2017-001-11 (Project Name: Development of fusion technology for Radar wind profiler).

Acknowledgments: We would like to thank the editor and three anonymous reviewers for their comments, which have greatly improved this manuscript. We thank the Korea Meteorological Administration for the dataset.

Conflicts of Interest: The authors declare no conflict of interest.

References

1. Chen, T.-J.G.; Chang, C.-P. The structure and vorticity budget of an early summer monsoon trough (Mei-Yu) over Southeastern China and Japan. *Mon. Weather Rev.* **1980**, *108*, 942–953. [CrossRef]
2. Park, S.U.; Yoon, I.H.; Chung, S.K. Heat and moisture sources associated with the Changma Front during the summer of 1978. *Asia Pac. J. Atmos. Sci.* **1986**, *22*, 1–27.
3. Ding, Y. Summer monsoon rainfalls in China. *J. Meteorol. Soc. Jpn. Ser. II* **1992**, *70*, 373–396. [CrossRef]
4. Ding, Y.; Chan, J.C.L. The East Asian summer monsoon: An overview. *Meteorol. Atmos. Phys.* **2005**, *89*, 117–142.
5. Houze, R.A. *Cloud Dynamics*; Elsevier Science: Amsterdam, The Netherlands, 2014; ISBN 0080921469.
6. Bluestein, H.B.; Jain, M.H.; Bluestein, H.B.; Jain, M.H. Formation of mesoscale lines of pirecipitation: Severe squall lines in Oklahoma during the spring. *J. Atmos. Sci.* **1985**, *42*, 1711–1732. [CrossRef]
7. Jeong, J.-H.; Lee, D.-I.; Wang, C.-C.; Jang, S.-M.; You, C.-H.; Jang, M. Article in annales geophysicae. *Ann. Geophys.* **2012**, *30*, 1235–1248. [CrossRef]
8. Rasmussen, E.N.; Blanchard, D.O.; Rasmussen, E.N.; Blanchard, D.O. A baseline climatology of sounding-derived supercell and tornado forecast parameters. *Weather Forecast.* **1998**, *13*, 1148–1164. [CrossRef]
9. Thompson, R.L.; Edwards, R.; Hart, J.A.; Elmore, K.L.; Markowski, P.; Thompson, R.L.; Edwards, R.; Hart, J.A.; Elmore, K.L.; Markowski, P. Close proximity soundings within supercell environments obtained from the rapid update cycle. *Weather Forecast.* **2003**, *18*, 1243–1261. [CrossRef]
10. Thompson, R.L.; Mead, C.M.; Edwards, R. Effective storm-relative helicity and bulk shear in supercell thunderstorm environments. *Weather Forecast.* **2007**, *22*, 102–115. [CrossRef]
11. Kim, D.-W.; Kim, Y.-H.; Kim, K.-H.; Shin, S.-S.; Kim, D.-K.; Hwang, Y.-J.; Park, J.-I.; Choi, D.-Y.; Lee, Y.-H. Atmospheric vertical structure of heavy rainfall system during the 2010 summer intensive observation period over Seoul metropolitan area. *J. Korean Earth Sci. Soc.* **2012**, *33*, 148–161. [CrossRef]
12. Kim, K.-H.; Kim, Y.-H.; Jang, D.-E. The analysis of Changma structure using radiosonde observational data from KEOP-2007: Part II. The dynamic and thermodynamic characteristics of Changma in 2007. *Korean Meteorol. Soc.* **2009**, *19*, 297–307.
13. Weber, B.L.; Wuertz, D.B.; Strauch, R.G.; Merritt, D.A.; Moran, K.P.; Law, D.C.; van de Kamp, D.; Chadwick, R.B.; Ackley, M.H.; Barth, M.F.; et al. Preliminary evaluation of the first NOAA demonstration network wind profiler. *J. Atmos. Ocean. Technol.* **1990**, *7*, 909–918. [CrossRef]
14. Barth, M.F.; Chadwick, R.B.; van de Kamp, D.W. Data processing algorithms used by NOAA's wind profiler demonstration network. *Ann. Geophys.* **1994**, *12*, 518–528. [CrossRef]
15. Nash, J.; Oakley, T.J. Development of COST 76 wind profiler network in Europe. *Phys. Chem. Earth Part B* **2001**, *3*, 193–199. [CrossRef]
16. Ishihara, M.; Kato, Y.; Abo, T.; Kobayashi, K.; Izumikawa, Y. Characteristics and performance of the operational wind profiler network of the Japan meteorological agency. *J. Meteorol. Soc. Jpn. Ser. II* **2006**, *84*, 1085–1096. [CrossRef]
17. Kim, K.-H.; Kim, M.-S.; Seo, S.-W.; Kim, P.-S.; Kang, D.-H.; Kwon, B.H. Quality evaluation of wind vectors from UHF wind profiler using radiosonde measurements. *J. Environ. Sci. Int.* **2015**, *24*, 133–150. [CrossRef]
18. Sakazaki, T.; Fujiwara, M. Diurnal variations in lower-tropospheric wind over Japan part I: Observational results using the wind profiler network and data acquisition system (WINDAS). *J. Meteorol. Soc. Jpn.* **2010**, *88*, 325–347. [CrossRef]
19. Campistron, B.; Puygrenier, V.; Bénech, B.; Lohou, F.; Saïd, F.; Cousin, F.; Dupont, E. Trajectory derived from the 3d linear wind field retrieved by a wind-profiler mesoscale network. In Proceedings of the 16th Symposium on Boundary Layers and Turbulence and 13th Conference on Interactions of the Sea and Atmosphere, Portland, OR, USA, 8 August 2004.
20. Saïd, F.; Campistron, B.; Delbarre, H.; Canut, G.; Doerenbecher, A.; Durand, P.; Fourrié, N.; Lambert, D.; Legain, D. Offshore winds obtained from a network of wind-profiler radars during HyMeX. *Q. J. Meteorol. Soc.* **2016**, *142*, 23–42. [CrossRef]

21. Jain, M.; Zhongqi, J.; Zahrai, A.; Dodson, A.; Burcham, H.; Priegnitz, D.; Smith, S. Software architecture of the NEXRAD open systems radar product generator (ORPG). In Proceedings of the IEEE 1997 National Aerospace and Electronics Conference. NAECON 1997, Dayton, OH, USA, 14–17 July 1997; Volume 1, pp. 308–313.
22. Waldteufel, P.; Corbin, H.; Waldteufel, P.; Corbin, H. On the analysis of single-doppler radar data. *J. Appl. Meteorol.* **1979**, *18*, 532–542. [CrossRef]
23. Kim, M.-S.; Kwon, B.H. Rainfall detection and rainfall rate estimation using microwave attenuation. *Atmosphere* **2018**, *9*, 287. [CrossRef]
24. Neumann, P.P.; Bartholmai, M. Real-time wind estimation on a micro unmanned aerial vehicle using its inertial measurement unit. *Sens. Actuators A Phys.* **2015**, *235*, 300–310. [CrossRef]
25. Garratt, J.R. Review: The atmospheric boundary layer. *Earth Sci. Rev.* **1994**, *37*, 89–134. [CrossRef]
26. Ahn, M.-H.; Won, H.Y.; Han, D.; Kim, Y.-H.; Ha, J.-C. Characterization of downwelling radiance measured from a ground-based microwave radiometer using numerical weather prediction model data. *Atmos. Meas. Tech.* **2016**, *9*, 281–293. [CrossRef]
27. White, A.B.; Senff, C.J.; Keane, A.N.; Darby, L.S.; Djalalova, I.V.; Ruffieux, D.C.; White, D.E.; Williams, B.J.; Goldstein, A.H. A wind profiler trajectory tool for air quality transport applications. *J. Geophys. Res. Atmos.* **2006**, *111*. [CrossRef]
28. Blanchard, D.O. Assessing the vertical distribution of convective available potential energy. *Weather Forecast.* **1998**, *13*, 870–877. [CrossRef]
29. Moncrieff, M.W.; Miller, M.J. The dynamics and simulation of tropical cumulonimbus and squall lines. *Q. J. R. Meteorol. Soc.* **1976**, *102*, 373–394. [CrossRef]
30. Stull, R.B. *An Introduction to Boundary Layer Meteorology*; Springer: Dordrecht, The Netherlands, 1988; ISBN 9400930275.
31. Droegemeier, K.K.; Lazarus, S.M.; Davies-Jones, R. The influence of helicity on numerically simulated convective storms. *Mon. Weather Rev.* **1993**, *121*, 2005–2029. [CrossRef]
32. Markowski, P.M.; Straka, J.M.; Rasmussen, E.N.; Blanchard, D.O.; Markowski, P.M.; Straka, J.M.; Rasmussen, E.N.; Blanchard, D.O. Variability of storm-relative helicity during VORTEX. *Mon. Weather Rev.* **1998**, *126*, 2959–2971. [CrossRef]
33. Arya, S.P. *Introduction to Micrometeorology*; Academic Press: San Diego, CA, USA, 2001; ISBN 9788578110796.
34. Palomaki, R.T.; Rose, N.T.; van den Bossche, M.; Sherman, T.J.; De Wekker, S.F.J.; Palomaki, R.T.; Rose, N.T.; van den Bossche, M.; Sherman, T.J.; Wekker, S.F.J. De wind estimation in the lower atmosphere using multirotor aircraft. *J. Atmos. Ocean. Technol.* **2017**, *34*, 1183–1191. [CrossRef]
35. Colquhoun, J.R.; Riley, P.A.; Colquhoun, J.R.; Riley, P.A. Relationships between tornado intensity and various wind and thermodynamic variables. *Weather Forecast.* **1996**, *11*, 360–371. [CrossRef]
36. Kerr, B.W.; Darkow, G.L.; Kerr, B.W.; Darkow, G.L. Storm-relative winds and helicity in the tornadic thunderstorm environment. *Weather Forecast.* **1996**, *11*, 489–505. [CrossRef]
37. Richardson, Y.P.; Droegemeier, K.K.; Davies-Jones, R.P.; Richardson, Y.P.; Droegemeier, K.K.; Davies-Jones, R.P. The influence of horizontal environmental variability on numerically simulated convective storms. Part I: Variations in vertical shear. *Mon. Weather Rev.* **2007**, *135*, 3429–3455. [CrossRef]
38. Kumjian, M.R.; Ryzhkov, A.V.; Kumjian, M.R.; Ryzhkov, A.V. Storm-relative helicity revealed from polarimetric radar measurements. *J. Atmos. Sci.* **2009**, *66*, 667–685. [CrossRef]
39. Kim, K.-H. Retrieval of Three Dimensional Wind Fields Using Data of UHF Wind Profiler Network. Ph.D. Thesis, Pukyong National University, Busan, Korea, 2017.
40. Kim, P.-S.; Kim, K.-H.; Campistron, B.; Yoon, H.-J.; Kwon, B.H. UHF and S-band radar networks. *J. Korea Inst. Electron. Commun. Sci.* **2018**, *13*, 305–312.
41. Kwon, B.H.; Kim, K.-H.; Seo, S.-W.; Campistron, B.; Saïd, F. *Wind Profiler and Weather Radar Networks in Korea: Presentation and Assessment*; Atelier Experimentation Instrumentation: Toulouse, France, 2014.